NGC 7793 P9: An Ultraluminous X-Ray Source Evolved from a Canonical Black Hole X-Ray Binary

Chin-Ping Hu[1] , Albert K. H. Kong[2] , C.-Y. Ng[1] , and K. L. Li[3]
[1] Department of Physics, The University of Hong Kong, Pokfulam Road, Hong Kong; cphu@hku.hk
[2] Institute of Astronomy, National Tsing Hua University, Hsinchu 30013, Taiwan
[3] Department of Physics and Astronomy, Michigan State University, East Lansing, MI 48824, USA

Abstract

Transient ultraluminous X-ray sources (ULXs) provide an important link bridging transient low-mass X-ray binaries and ULXs. Here we report the first discovery of both a canonical sub-Eddington outburst and an ultraluminous super-Eddington outburst from an unusual transient ULX, NGC 7793 P9, with a variability factor higher than 10^3. Its X-ray spectrum switches between the typical high/soft state and the steep power-law state during the canonical outburst. The inner radius of the accretion disk and the disk temperature–luminosity correlation suggest that P9 harbors a stellar-mass black hole (BH). At the beginning of the ultraluminous outburst, we observe a cool outer disk with a hard Comptonized spectrum, implying a transition to the ULX regime. When the luminosity increases to $L \gtrsim 3 \times 10^{39}$ erg s^{-1}, P9 shows a significantly curved spectrum that can be described by either a slim disk or a strongly curved Comptonized corona. The phenomenological model suggests that the hot disk observed near the peak of the ultraluminous outburst is coincidentally consistent with the extension of the thermal track. Utilizing more physical Comptonized disk models, we suggest that the corona cools down and the apparent disk-like spectrum is dominated by soft Comptonization. The significant variability above 1 keV supports this two-component scenario. The spectral evolution can also be interpreted with the supercritical accretion model. All these indicate that a canonical BH X-ray binary can show properties of a ULX.

Key words: accretion, accretion disks – black hole physics – X-rays: binaries – X-rays: individual (NGC 7793 P9)

1. Introduction

Accreting black holes (BHs) are bright X-ray sources powered by the gravitational potential energy of accreting materials. The luminosities of Galactic BHs are strongly limited to the Eddington luminosity (L_{Edd}), at which the radiation pressure balances the inward gravitational force of the accreting materials. Thanks to the revolution in astronomical instrumentation over the past several decades, the discovery of ultraluminous X-ray sources (ULXs) challenged the Eddington limit (see reviews by Frank et al. 2002; Feng & Soria 2011; Kaaret et al. 2017). ULXs are extragalactic off-nuclear X-ray point sources with luminosities exceeding the Eddington limit of a stellar-mass BH. Most ULXs are believed to be powered by stellar-mass BHs with mild beaming and/or moderate super-Eddington accretion rates. They show ultraluminous states distinct from the canonical spectral states of BH X-ray binaries (BHXBs; Gladstone et al. 2009; Feng & Soria 2011; Kaaret et al. 2017). Unlike the spectral behavior of a BHXB in the steep power-law (SPL) state that shows a hot disk and an optically thin corona, a genuine ULX usually shows a much cooler disk with a larger inner radius plus an optically thick corona and has a luminosity of $L \gtrsim 3 \times 10^{39}$ erg s^{-1}. ULX states can be further divided into the hard ultraluminous (HUL), soft ultraluminous (SUL), and supersoft ultraluminous spectral states (Sutton et al. 2013; Kaaret et al. 2017). In addition, those low-luminosity ULXs with $L \lesssim 3 \times 10^{39}$ erg s^{-1} usually show a curved spectrum that can be described with a broadened disk (BD) model, implying that the disk component is no longer a geometrically thin accretion disk but the luminosity remains sub-Eddington (Sutton et al. 2013).

The best studied ULXs are persistent sources with low variability factors (Feng & Kaaret 2006; Kaaret & Feng 2009). A stable high mass accretion rate is necessary to interpret the long

lifetime of the ultraluminous state. As long as the companion star of a ULX is a massive star with $M \gtrsim 10 M_\odot$, super-Eddington mass transfer occurs when the companion evolves to the Hertzsprung gap without a common envelope (King et al. 2001; Rappaport et al. 2005; Pavlovskii et al. 2017). Most of the currently known ULXs, including the ultraluminous pulsar P13 in NGC 7793, have early-type companions with high optical luminosities (Bachetti et al. 2014; Motch et al. 2014; Lau et al. 2016). It has also been proposed that some ULXs may exhibit a low-mass companion and be powered by a long-lasting super-Eddington outburst (King 2002). In contrast, BHXBs with low-mass companions are usually transient X-ray sources. Therefore, transient ULXs is key to testing this scenario and showing that a low-mass X-ray binary (LMXB) can evolve to a ULX with typical UL spectral behaviors. The Galactic LMXBs GRS 1915+105 and XTE J1550−564 showed optically thick Comptonized spectra during the peak of the outburst with a luminosity of $\sim 10^{39}$ erg s^{-1}. They could fill in the link bridging BHXBs and ULXs (Kubota & Done 2004; Soria 2007; Vierdayanti et al. 2010). Several transient ULXs were reported as evolved from canonical BHXBs although they showed either canonical BHXB spectral states or ultraluminous outburst only (see, e.g., Middleton et al. 2012; Kaaret & Feng 2013). Therefore, it remains unclear whether a canonical BHXB showing sub-Eddington outbursts can evolve into a ULX with a much higher luminosity and typical UL spectral behaviors. In this paper, we report the discovery of a transient ULX, NGC 7793 P9 (hereafter P9), that showed both a canonical BHXB outburst and an ultraluminous outburst that fill in the gap.

NGC 7793 is an SA(s)d type galaxy in the Sculptor Group with a distance of 3.6–3.9 Mpc (Karachentsev et al. 2003; Radburn-Smith et al. 2011; Crowther 2013; Tully et al. 2016). It has a bulge with filamentary spiral structures and several H II

regions (Read & Pietsch 1999). P9 is located at the northeast edge of one filament extending from the host galaxy and has no obvious association with any H II regions or supernova remnants (Read & Pietsch 1999). P9 was first characterized as a highly variable point source in a *ROSAT* survey (Read & Pietsch 1999). The X-ray spectrum of P9 was well fit with either a PL or a thermal bremsstrahlung model. The absorption column density (N_H) was rather large. A deep *Chandra* observation (ObsID 3954) revealed a faint source, CXOU J235808.7−323403, at the position of P9, but its spectrum was not well characterized (Pannuti et al. 2011). Therefore, the luminosity was not well constrained. By simply assuming a PL with a photon index $\Gamma = 1.5$ and $N_H = 1.15 \times 10^{20}\,cm^{-2}$, the luminosity of P9 was estimated to be $4.5 \times 10^{37}\,erg\,s^{-1}$. No optical or radio counterparts have been found (Read & Pietsch 1999; Pannuti et al. 2011).

We report a detailed analysis of the transient ULX P9 based on *Neil Gehrels Swift* (hereafter *Swift*) monitoring data and several dedicated observations made with *Chandra*, *XMM-Newton*, and *NuSTAR*. We introduce the observation and data analysis in Section 2. The detailed spectral analysis, including the variability of Γ, the stacked *Swift* spectroscopy, and tests of more physical models during the ultraluminous outburst are presented in Section 3. We further discuss the implications of the spectral variability, especially the evolution of the disk component and the accretion models, in the super-Eddington accretion regime in Section 4. Finally, we summarize this work in Section 5.

2. Observations and Data Reduction

2.1. Swift *Observations*

The host galaxy NGC 7793 has been monitored with *Swift* since 2010. Four series of observations have been carried out in late 2010, from mid 2011 to late 2013, in late 2014, and from 2016 April to 2017 June. We extracted the XRT light curve with the online XRT pipeline[4] (Evans et al. 2007, 2009). P9 is clearly detected in 88 of the total 122 observations. We converted the 0.3–10 keV count rates to the luminosities with WebPIMMS[5] by assuming $N_H = 10^{21}\,cm^{-2}$, a PL spectrum with $\Gamma = 2$, and a distance of 3.9 Mpc. We will show that Γ varied between ∼1.5 and ∼2.5 in a later section. The value $\Gamma = 2$ is a conventional average value to estimate the luminosity variability in Figure 1. We searched for periodic signals between $P = 10$–1000 days to check if P9 contained orbital or superorbital modulations like other ultraluminous pulsars but we did not find significant periodicity (Kong et al. 2016; Walton et al. 2016; Hu et al. 2017). The luminosity of P9 varied between ∼10^{38} and ∼$10^{39}\,erg\,s^{-1}$, well below the ULX regime before 2013 (see Figure 1). Interestingly, P9 showed an ultraluminous outburst with a peak luminosity of ∼$5 \times 10^{39}\,erg\,s^{-1}$ after 2014, and the luminosity returned to $\lesssim 10^{39}\,erg\,s^{-1}$ in 2017. We further downloaded all of the *Swift* UVOT images taken between 2010 and 2017, and stacked them to obtain deep UV images in four *Swift* bands (*u*, *w1*, *m2*, and *w2*). No UV counterpart was seen within the error circle of the *Chandra* position.
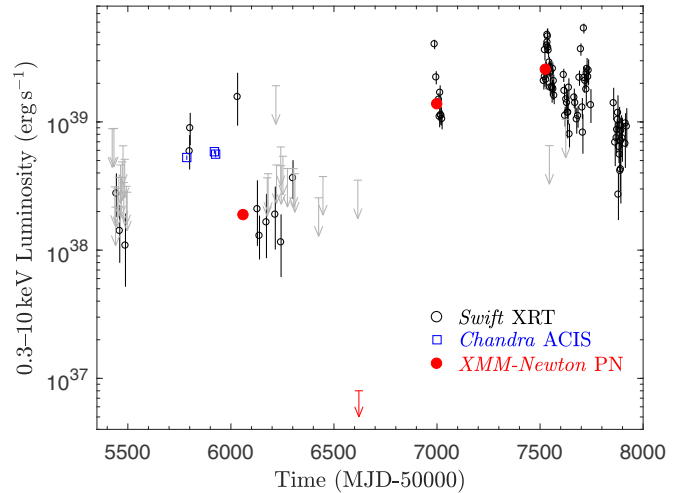

Figure 1. *Swift* XRT light curve of NGC 7793 P9. The black diamonds are the data points determined with *Swift* XRT, where the gray crosses denote the upper limits. The *Chandra* (blue squares) and *XMM-Newton* (red filled circles) data are also plotted on the same figure.

2.2. Chandra *Data*

NGC 7793 was observed with *Chandra* in 2003 (C1: ObsID 3954) and 2011 (C2: ObsID 14231, C3: ObsID 13439, C4: ObsID 14378). The observation log of P9 is listed in Table 1. These four observations were made with the Advanced CCD Imaging Spectrometer array (ACIS-S) in the timed exposure mode. We reprocessed the data using the pipeline chandra_repro in the *Chandra* Interactive Analysis of Observations (CIAO) version 4.9 with the most recent calibration database (CALDB) version 4.7.3 (Fruscione et al. 2006). We extracted the source events from a circular aperture of 2″ radius. The background events were extracted from a nearby source-free region. We estimated the source luminosity with the srcflux command and plotted the results in Figure 1. The luminosities of the 2011 observations are ∼$5 \times 10^{38}\,erg\,s^{-1}$, consistent with the *Swift* light curve.

We extracted the light curves of P9 to check for any variability in each observation. We used the task dmextract to create the background-subtracted light curves, and the results are plotted in Figure 2. The light curves show limited fluctuations, and no significant trends were observed.

2.3. XMM-Newton *Data*

XMM-Newton has observed NGC 7793 nine times with the EPIC CCD in the full-frame mode, and four of them are publicly available. We reduced the data using the *XMM-Newton* Science Analysis Software (SAS version 16.0.0) and used epproc and emproc to reprocess the PN and MOS data with the latest calibration files, respectively. We filtered out the time intervals with a flaring particle background. The effective exposure times are listed in Table 1. The 2012 observation (X1: ObsID 0693760101) shows that the luminosity of P9 was ∼$2 \times 10^{38}\,erg\,s^{-1}$. In 2013, P9 was not detected with *XMM-Newton* (X2: ObsID 0693760401). We estimated a 3σ upper limit as ∼$8 \times 10^{36}\,erg\,s^{-1}$. On the other hand, P9 was very bright with luminosities exceeding $10^{39}\,erg\,s^{-1}$ in 2014 (X3: ObsID 0748390901) and 2016 (X4: ObsID 0781800101). The nondetection of P9 in 2013 suggests that P9 was in quiescence, and the entire time span can be divided into two epochs: a less

Table 1
Observation Log of NGC 7793 P9

Epoch	Observatory	ObsID	Instrument	MJD	Exposure[a] (ks)
C1	*Chandra*	3954	ACIS-S	52889	49
C2	*Chandra*	14231	ACIS-S	55787	59
C3	*Chandra*	13439	ACIS-S	55920	58
C4	*Chandra*	14378	ACIS-S	55926	25
X1	*XMM-Newton*	0693760101	PN	56061	23
			MOS		36
X2	*XMM-Newton*	0693760401	PN	56621	46
			MOS		48
X3	*XMM-Newton*	0748390901	PN	57002	47
			MOS		49
X4[b]	*XMM-Newton*	0781800101	PN	57528	24
			MOS		48
	NuSTAR	80201010002	FPMA+FPMB	57528	114

Notes.
[a] Effective exposure time after filtering out the time intervals with a flaring background.
[b] A joint observation with *NuSTAR*.

luminous outburst from 2011 to 2012 and an ultraluminous outburst from 2014.

We then extracted the background-subtracted light curves of P9 from individual observations. We extracted the source events from a circular aperture of $15''$ radius to minimize the possible contamination from CXOU J235810.4−323357 (Pannuti et al. 2011). We used `epiclccorr` to subtract the background light curve and apply the relative and absolute corrections. Figure 2 shows the light curves of the *XMM-Newton* observations. No significant variability was seen in the X1 and X3 data sets. However, the light curve of X4 shows a decreasing trend. We calculated the fractional variability (F_{var}) for X3 and X4 in which P9 was bright enough. F_{var} can be defined as

$$F_{var} = \frac{1}{\langle X \rangle} \sqrt{S^2 - \langle \sigma_{err}^2 \rangle}, \quad (1)$$

where S^2 is the total variance of the light curve, $\langle \sigma_{err}^2 \rangle$ is the mean square of the uncertainty of each data point, and $\langle X \rangle$ is the mean count rate (Edelson et al. 2002). For individual data sets, we calculated F_{var} for the full energy range (0.3–10 keV), the soft X-ray band (0.3–1 keV), and the hard X-ray band (1–10 keV). We did not observe significant variability in all three bands of X3, and the 2σ upper limit is estimated as $F_{var} < 0.06$. On the other hand, X4 shows a clear variability with $F_{var} = 0.12 \pm 0.01$ in 0.3–10 keV, and the variability is dominated by the X-ray emission in 1–10 keV with $F_{var} = 0.15 \pm 0.02$. F_{var} in the 0.3–1 keV band was less obvious with a value of 0.05 ± 0.02. We corrected the photon arrival time to the solar barycenter and searched for periodicity in the range of 0.1–1000 s with both the *H*-test (de Jager et al. 1989) and the Fourier analysis, but no periodicity was found.

2.4. NuSTAR Data

NGC 7793 was observed with both *NuSTAR* and *XMM-Newton* on 2016 May 20 (ObsID 80201010002). We reduced the data using the *NuSTAR* analysis software NUSTARDAS (version 1.9.1) with the calibration database of version

20170614. We used the script `nupipeline` to apply data calibration and screening, and then extracted the images, light curves, and spectra using `nuproducts`. The X-ray emission of P9 was detected with both the FPMA and FPMB below ∼20 keV. Figure 3 shows the stacked images obtained by all of the *XMM-Newton* EPIC detectors in the 0.3–10 keV band, and *NuSTAR* FPMA+FPMB in the 3–10 keV, 10–20 keV, and 20–79 keV ranges. The emission of P9 is dominated by soft X-rays below 10 keV. For the 10–20 keV band, P9 was marginally detected with a detection significance of 8.8σ using the wavelet source detection algorithm `wavdetect`.

We extracted the light curve of each *NuSTAR* orbit to check if P9 showed long-term variability. We extracted the source events from a circular aperture of $60''$ radius and background events from an annulus with an inner radius of $80''$ and an outer radius of $120''$. The result is plotted in Figure 2 together with the scaled X4 light curve obtained with *XMM-Newton*. The *NuSTAR* flux dropped significantly after ∼MJD 57529.5.

3. X-Ray Spectroscopy

We started the spectral analysis with the *Chandra*, *XMM-Newton*, and *NuSTAR* data sets, which have much better signal-to-noise ratios than the *Swift* data sets. We used the absorption model `tbnew`[6] (Wilms et al. 2000), fixed the Galactic absorption column density to $N_H(gal) = 1.23 \times 10^{20}$ cm^{-2}, and set an additional absorption for the external galaxy (Kalberla et al. 2005). We followed the empirical classification strategy of ULX spectral states proposed by Sutton et al. (2013). We first employed simple phenomenological models, the multicolor disk blackbody (MCD; Mitsuda et al. 1984) and the power-law (PL), to fit the spectra. Then, we tried a combination of them (MCD+PL) to check if adding an additional component improves the fit. For this case, we further check the empirical classification of the UL spectra by computing the photon index (Γ) and the fraction of the PL flux in 0.3–1 keV. After that, we fit the spectrum with more physical models like the slim disk and the Comptonized models to further characterize the spectral behaviors of those data sets

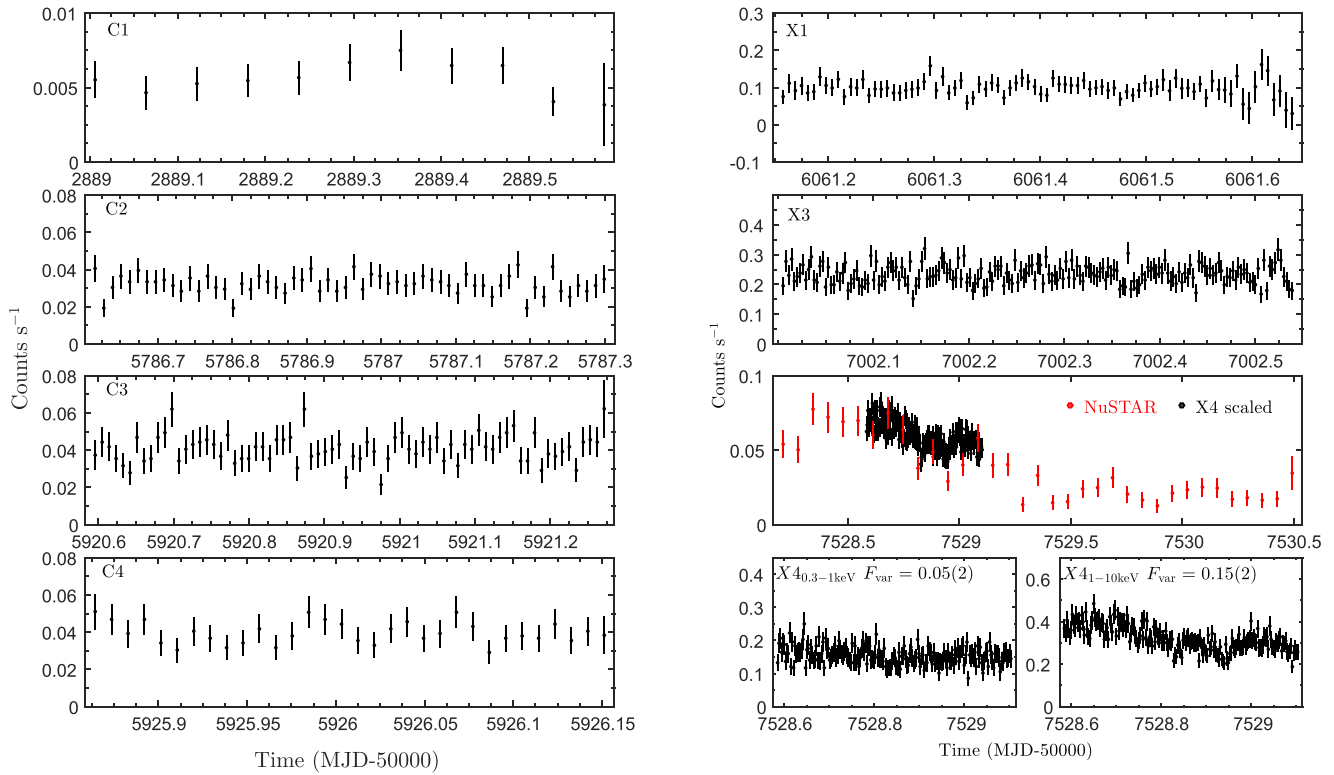---

Figure 2. (Left) *Chandra* 0.5–7 keV light curves of NGC 7793 P9. (Right) *XMM-Newton* (0.3–10 keV) and *NuSTAR* (3–79 keV) light curves of NGC 7793 P9. The X4 light curve on the third panel was scaled to fit the *NuSTAR* count rate. The bottom panel showed the soft (0.1–1 keV) and hard (1–10 keV) X-ray light curves of the X4 observation.
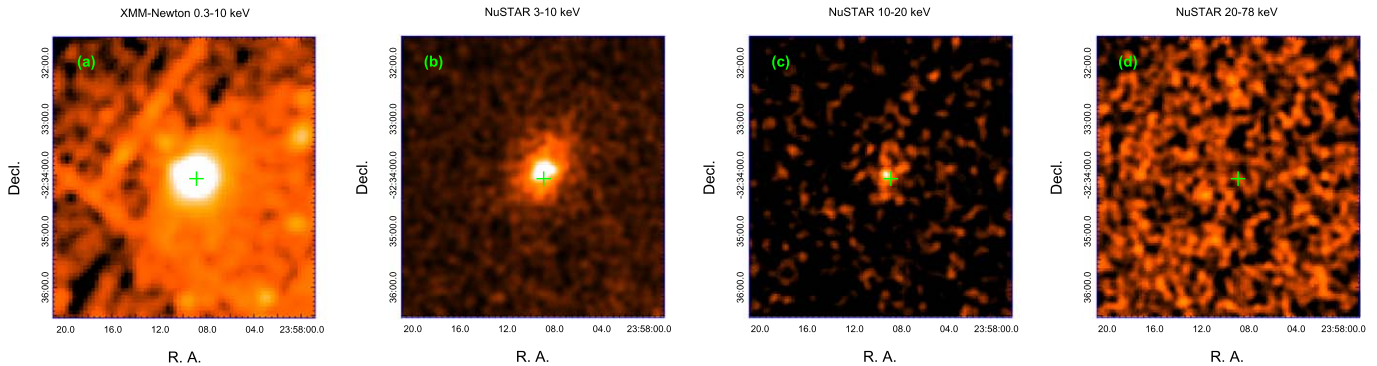

Figure 3. X-ray images of NGC 7793 P9 obtained with (a) *XMM-Newton* in 0.3–10 keV, and *NuSTAR* in (b) 3–10 keV, (c) 10–20 keV, and (d) 10–79 keV. The *XMM-Newton* image is stacked from the MOS1, MOS2, and PN images, and the *NuSTAR* images are combined from the FPMA and FPMB images. The green cross denotes the *Chandra* position of P9.

with the UL spectral features. The best-fit parameters for each *Chandra* and *XMM-Newton* observations with a simple MCD +PL model were summarized in Table 2.

3.1. Phenomenological Models

3.1.1. Chandra *Spectroscopy*

The *Chandra* 0.5–7 keV spectra were generated using the `specextract` command, which creates source and background spectra, corresponding response files (rmf), and ancillary files (arf). The spectra were then grouped to a minimum of 15 photons per bin for C1 and 25 photons per bin for C2–C4 for spectral fitting. The C1 observation made in

2003 can be well described with a simple PL but $N_{\rm H} = 1.3^{+1.7}_{-1.3} \times 10^{21}$ cm^{-2} is not well constrained. The uncertainties of the spectral parameters are obtained within a 90% confidence interval. The photon index is $\Gamma = 2.4^{+0.5}_{-0.4}$, which is quite soft but with a large uncertainty. To doubly confirm the result obtained with the χ^2 statistic, we tried the Cash statistic without grouping the photons and yielded a consistent result (Cash 1979). The C2 spectrum is well fit by the MCD with an inner-disk temperature $kT_{\rm in} = 0.96^{+0.07}_{-0.06}$ keV. The normalization constant indicates an apparent inner radius of $R_{\rm in}\sqrt{\cos\theta} \approx 50$ km, where θ is the inclination angle. We tried the MCD+PL model but obtained no significant improvement. The C3 and C4 observations were taken four months after the C2

Table 2
Best-fit Spectral Parameters of NGC 7793 P9 obtained from the *Chandra*, *XMM-Newton*, and *NuSTAR* Data Sets

Obs.	Model	$L_{0.3–10\,\mathrm{keV}}$ $(10^{39}\,\mathrm{erg\,s^{-1}})$	L_{MCD} $(10^{39}\,\mathrm{erg\,s^{-1}})$	N_{H} $(10^{22}\,\mathrm{cm^{-2}})$	$R_{\mathrm{in}}\sqrt{\cos\theta}$ (km)	kT_{in} (keV)	Γ	χ^2/dof	State
C1	PL	$0.10^{+0.03}_{-0.02}$	⋯	$0.13^{+0.17}_{-0.13}$	⋯	⋯	$2.4^{+0.5}_{-0.4}$	6.8/14	SPL
C2	MCD	0.5 ± 0.1	0.5 ± 0.1	0.07 ± 0.04	49^{+7}_{-6}	$0.96^{+0.07}_{-0.06}$	⋯	62.7/57	Thermal
C3	PL	0.79 ± 0.06	⋯	0.09 ± 0.04	⋯	⋯	2.2 ± 0.1	62.2/67	SPL
C4	PL	$0.83^{+0.10}_{-0.08}$	⋯	$0.14^{+0.08}_{-0.07}$	⋯	⋯	2.3 ± 0.02	27.1/31	SPL
X1	MCD	$0.26^{+0.08}_{-0.07}$	$0.26^{+0.08}_{-0.07}$	$0.024^{+0.018}_{-0.014}$	53^{+8}_{-7}	0.78 ± 0.02	⋯	77.8/93	Thermal
X3	MCD+PL	1.1 ± 0.2	$0.36^{+0.07}_{-0.08}$	0.07 ± 0.02	370^{+90}_{-60}	0.34 ± 0.04	1.8 ± 0.2	171.9/189	UL (HUL)
X4[a]	MCD+PL	$3.4^{+0.6}_{-0.4}$	$1.4^{+0.4}_{-0.4}$	$0.11^{+0.03}_{-0.02}$	34^{+7}_{-6}	1.5 ± 0.2	$2.0^{+0.2}_{-0.1}$	308.3/311	UL (BD?)
	MCD+PL[b]	4^{+5}_{-2}	$0.6^{+0.8}_{-0.4}$	0.06 ± 0.04	100^{+90}_{-60}	$0.8^{+0.5}_{-0.2}$	$1.4^{+0.4}_{-0.8}$	302.1/309	

Notes.
[a] The *NuSTAR* data set was also included in the fitting.
[b] A high-energy cutoff was included in this PL component with a cutoff energy of 4^{+1}_{-4} keV and the folding energy of 5 ± 5 keV.

observation and had a time separation of five days. An absorbed PL model with $\Gamma \approx 2.3$ and $N_{\mathrm{H}} \sim 10^{21}\,\mathrm{cm^{-2}}$ can well describe both spectra, and adding an MCD does not improve the fit statistic significantly. All of the *Chandra* spectra and the corresponding best-fit models are shown in Figure 4. It is clear that the C2 spectrum, which was best described with an MCD model, has a stronger curvature than the other three data sets that can be described by a PL model. We checked the spectral fits with Cash statistics, and the results are fully consistent with those obtained with χ^2 statistics.

3.1.2. XMM-Newton *Spectroscopy*

To extract high-quality *XMM-Newton* spectra, we filtered out the background flaring epochs and chose the events with good grades by restricting `FLAG = 0`. We set `PATTERN ⩽ 4` for the PN data and `PATTERN ⩽ 12` for the MOS data. The source and background regions were normalized using the `back-scale` command, and the corresponding response files and ancillary files were created using `rmfgen` and `arfgen`. The spectra were then grouped to a minimum of 15 photons per bin for X1 and 25 photons per bin for the X3 and X4 observations using `specgroup`.

We fit the PN, MOS1, and MOS2 spectra in 0.3–10 keV simultaneously with all the parameters tied between instruments. To further correct for any differences in calibrations between the detectors, we added an overall normalization constant for the MOS1 and MOS2 spectra. The discrepancies in the following analysis are well below ≲5%. The X1 observation was taken in the tail of the canonical outburst, roughly five months after the *Chandra* C3 and C4 observations. The spectra can be well described with an MCD model. The best-fit kT_{in} is 0.79 ± 0.06 keV, and the apparent inner radius of the accretion disk is $R_{\mathrm{in}}\sqrt{\cos\theta} = 53^{+9}_{-8}$ km, consistent with the C2 spectrum taken in 2011. Similar to all the *Chandra* observations, the fitting cannot be significantly improved by two-component or more complex models. The spectral change from C2 to X1 suggests that P9 had a canonical outburst in 2011–2012, and its spectrum switched between an MCD with an inner radius of ∼50 km and a PL with $\Gamma \sim 2.3$.

The X3 observation was made in the early phase of the ultraluminous outburst. We found that neither the MCD model nor the PL model provides acceptable fitting. On the other hand, a two-component MCD+PL model can significantly improve the fitting with a $\chi^2/\mathrm{dof} = 171.9/189$ (see Figure 4).

The best-fit N_{H} is $(7 \pm 2) \times 10^{20}\,\mathrm{cm^{-2}}$. The temperature and radius of the inner disk are $kT_{\mathrm{in}} = 0.34 \pm 0.04$ keV and $R_{\mathrm{in}}\sqrt{\cos\theta} = 370^{+90}_{-60}$ km, which imply a much cooler disk with an innermost radius much farther away from the central compact object compared to the canonical thermal and SPL states of a BHXB. The PL component has $\Gamma = 1.8(2)$, clearly harder than the value of the canonical SPL spectrum.

The X4 observation was made near the peak of the ultraluminous outburst. We included the *NuSTAR* 3–20 keV data in the fitting to increase the statistic and constrain the spectral behavior in the hard X-ray band. Since the *XMM-Newton* X4 observation was made before this drop, we extracted the *NuSTAR* spectra during the X4 observation time interval. We fit all five spectra (PN, MOS1, MOS2, FPMA, FPMB) simultaneously. Similar to the X3 observation, a two-component MCD+PL model provides a good statistic with $\chi^2/\mathrm{dof} = 308.3/311$. The disk temperature is $kT_{\mathrm{in}} = 1.5 \pm 0.2$ keV and $\Gamma = 2.0 \pm 0.2$. In the soft X-ray band, the apparent spectral curvature caused by a highly optically thick Comptonized component may be classified as a disk-like spectrum (Sutton et al. 2013). Therefore, we used an MCD plus PL with a high-energy cutoff to fit the data. The fitting statistic is equally good with a $\chi^2/\mathrm{dof} = 302.1/309$. The N_{H} value is $(7 \pm 4) \times 10^{20}\,\mathrm{cm^{-2}}$, consistent with that obtained in the previous section. The cutoff energy is 5 ± 5 keV, indicating a strong spectral curvature caused by an optically thick corona but not well constrained.

3.1.3. Determining the Extragalactic Absorption

Most of the best-fit models yield a similar N_{H} with a value of $(\sim 5–10) \times 10^{20}\,\mathrm{cm^{-2}}$. Therefore, we assume that N_{H} did not significantly vary during the entire observation time span. We fit all the *Chandra*, *XMM-Newton*, and *NuSTAR* data simultaneously with a tied N_{H} and their corresponding best-fit models to further constrain the N_{H}. The resulting χ^2/dof is 767.3/789, and N_{H} is determined as $(7 \pm 1) \times 10^{20}\,\mathrm{cm^{-2}}$. We also tried to use the abundances with the absorption model `phabs` with the corresponding abundance and obtained $N_{\mathrm{H}} = (6 \pm 1) \times 10^{20}\,\mathrm{cm^{-2}}$, slightly lower than that obtained with `tbnew` (Anders & Grevesse 1989). Other parameters are fully consistent with those listed in Table 2. The N_{H} is consistent with that of P13, indicating that P9 is unlikely a heavily absorbed source compared to other point sources in NGC 7793 (Israel et al. 2017b).
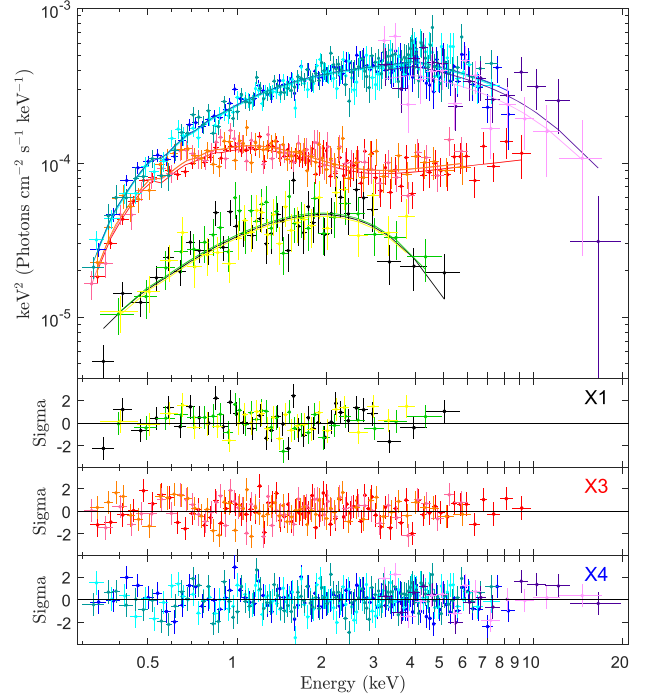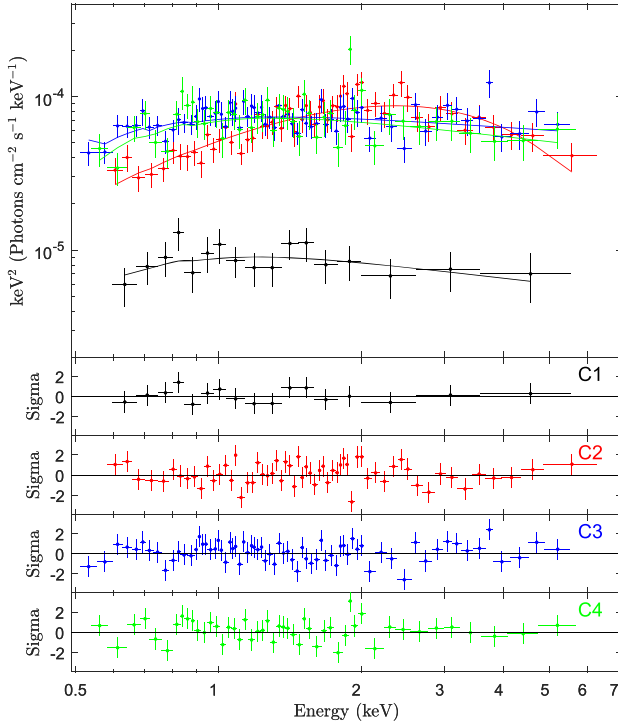
Figure 4. (Left) *Chandra* spectra of NGC 7793 P9. The black, red, blue, and green points represent the C1, C2, C3, and C4 spectra, respectively. The solid lines are the corresponding best-fit models. (Right) *XMM-Newton* and *NuSTAR* spectra of NGC 7793 P9. The solid lines are the corresponding best-fit MCD, MCD+PL, and DiskPBB models for the X1, X3, and X4 data sets, respectively.

3.2. More Physical Models

From the spectral shapes in Figure 4 and fitting parameters in Table 2, we noticed that the X3 and X4 spectra likely represent the ultraluminous states. X3 can be well described with a cool disk plus a hard PL without a significant high-energy cutoff below 10 keV. The spectral shape is similar to BHXB spectra in the low/hard state but the luminosity is much higher. This is the typical spectral feature of hard ULXs. The low $kT_{in} < 0.5$ keV and hard $\Gamma < 2$ implies an HUL spectrum according to the empirical classification (Sutton et al. 2013). The X4 spectrum is disk-like but much broader than a standard MCD. This spectrum can be classified as a BD. However, X4 shows a significant difference from X3 only above ~1 keV, implying that the major difference could be contributed by the PL tail. This heavily Comptonized spectra are sometimes misclassified as a BD. Hence, we carefully examine the X3 and X4 spectra with more physical Comptonized models and slim disk models to explore the underlying physics.

3.2.1. Slim Disk

We first fit X4 with a *p*-free accretion disk (DiskPBB), in which the radial advection is taken into account (Mineshige et al. 1994; Hirano et al. 1995). This model is an approximation of the slim disk. The radial temperature profile in this model has a PL dependence $T(r) \propto r^{-p}$, where r is the radius and p is a free parameter. A standard MCD corresponds to $p = 0.75$, and a slim disk can be approximated with $p < 0.75$. The best-fit χ^2/dof is 308.3/312, slightly better than the statistic of the MCD+PL model. The inner-disk temperature is $kT_{in} = 2.2 \pm 0.2$ keV, much higher than that in the high/soft state of the normal outburst (see Table 3). The low $p = 0.57 \pm 0.02$ is consistent with other ULXs with a BD spectrum (Kaaret

et al. 2017). The apparent inner radius, $R_{in}\sqrt{\cos\theta} = 16 \pm 3$ km, is extremely small. We further tried a table model for a slim disk (Kawaguchi 2003), which included corrections for local BB contribution, Comptonized spectrum, or relativistic effects. We found that the spectrum can be described by the model ID 4, which includes a slim disk and a Comptonized local spectrum. The resulting χ^2/dof is 304.7/311, which is equally good as the *p*-free disk model. The BH mass is $4^{+27}_{-2} M_\odot$, N_H is $(7 \pm 2) \times 10^{20}$ cm^{-2}, the mass accretion rate is $\dot{m} = 6^{+5}_{-1}$ L_{Edd}/c^2, but the viscosity is not well constrained. N_H is fully consistent with previous measurements. We also tried to use the *p*-free disk model to fit X3 spectra; however, the statistic is unacceptably high since the slim disk is unable to describe the high-energy tail. We therefore add a PL component and found that the disk component has a small value of p, but the uncertainty is large.

3.2.2. Comptonized Model: SIMPL

The disk corona usually contributes a high-energy tail in the X-ray spectrum of a BHXB. We described the tail with the convolution model SIMPL. This model empirically calculates the Comptonized spectrum from the scattering of a fraction of seed photons, i.e., the MCD component (Steiner et al. 2009). The seed photons are redistributed to both higher and lower energies. The normalization factor is the scattered fraction (f_{sc}). We fit the X3 data set, which results in an acceptable statistic of χ^2/dof = 172.9/189. The disk is partially scattered with a fraction of $f_{sc} = 0.33$ and has an apparent inner-disk temperature of $kT_{in} = 0.33 \pm 0.04$ keV and a radius of $R_{in}\sqrt{\cos\theta} = 500^{+160}_{-100}$ km. This result still shows a truncated disk similar to that obtained from phenomenological models.

We fit the X4 data with the same model, but the best-fit statistic ($\chi^2/\mathrm{dof} = 366.2/315$) is much worse than that yielded by MCD+PL. We obtained $f_{\rm sc} = 1$, implying that all disk photons are scattered to the Comptonized component. The seed MCD component has $kT_{\rm in} = 0.92 \pm 0.6$ keV and $R_{\rm in}\sqrt{\cos\theta} = 109^{+14}_{-12}$ km, a bit closer to the BH than that obtained from the X3 data set.

3.2.3. Comptonized Model: NTHCOMP

In addition to the convolution model, we used an additive Comptonized model, NTHCOMP, to describe the Comptonized continuum (Zdziarski et al. 1996; Życki et al. 1999). The high-energy rollover, which is sharper than an exponential cutoff, is parameterized by the electron temperature kT_e. We set the maximum seed photon temperature kT_{bb} to the inner-disk temperature $kT_{\rm in}$ of the MCD component. The statistic of X3 is insensitive to the electron temperature kT_e because no significant high-energy cutoff is observed below 10 keV. Hence, we fixed it to 100 keV. The fit statistic is acceptable, and the parameter suggests a cool disk with a large inner radius (see Table 3). The true disk radius can be re-estimated using the equation provided by Kubota & Makishima (2004) for the presence of disk Comptonization. Assuming an inclination angle of 60°, $R_{\rm in}$ can be estimated as 770^{+300}_{-140} km, slightly larger than that directly obtained from the MCD component.

The Comptonized component of X4 can also be described with this model. However, the normalization of the disk component is consistent with zero, implying that MCD is negligible. Therefore, we used NTHCOMP to fit the spectra and set kT_{bb} as a free parameter. The statistic is as good as that obtained from phenomenological models. The best-fit $kT_e = 1.9^{+0.5}_{-0.3}$ roughly corresponds to an exponential cutoff at 4–7 keV. This is consistent with that obtained from the MCD +PL model with a high-energy cutoff. The inner-disk radius can be re-estimated as 460^{+280}_{-140} km, consistent with that obtained from the X3 data set.

3.2.4. Disk–Corona Coupling: OPTXAGNF

The above two models account for the partial Comptonization of a standard MCD. However, the size of the corona may play an important role if the disk is only partially covered. The innermost accretion disk could be fully or partially Comptonized, while the outer disk remains standard and contributes a significant amount of soft X-ray emission. Done & Kubota (2006) proposed the DKBBFTH model to deal with the spectrum from the Comptonized corona over the inner disk. This model has been applied to the spectra of several ULXs to recover the properties of the inner disk (Gladstone et al. 2009). An upgraded model, OPTXAGNF, was proposed to fit the broadband spectra of narrow-line Seyfert 1 galaxies with the same aspect (Done et al. 2012). Given a similar accretion property, this model can be used to describe the UL and SPL states of BHXBs. The disk component is a canonical MCD where the radius is larger than the coronal radius. The disk inside the corona is not fully thermalized. Instead, the emission was Comptonized to form both soft excess and a hard PL tail. There are 11 parameters in OPTXAGNF: the BH mass ($M_{\rm BH}$), distance, luminosity in units of Eddington ratio ($\log L/L_{\rm Edd}$), BH spin (a), coronal radius ($R_{\rm cor}$ in units of $r_g = GM_{\rm BH}/c^2$), outer radius of the disk ($R_{\rm out}$), electron temperature (kT_e) and optical depth (τ) for the soft Comptonization component,

Table 3
Best-fit Spectral Parameters of the X3 and X4 Data Sets with More Physical Models

Model	Parameters	X3	X4
DiskPBB+PL	$N_{\rm H}$ (10^{22} cm^{-2})	0.12 ± 0.05	0.09 ± 0.02
	$T_{\rm in}$	$0.5^{+0.2}_{-0.1}$	2.2 ± 0.2
	$R_{\rm in}\sqrt{\cos\theta}$ (km)	120^{+190}_{-80}	16 ± 3
	p	$0.47^{+0.20}_{-0.06}$	0.57 ± 0.02
	Γ	$1.5^{+0.3}_{-0.5}$	…
	χ^2/dof	168.2/188	308.3/312
SIMPL(MCD)	$N_{\rm H}$ (10^{22} cm^{-2})	0.05 ± 0.02	0.007 ± 0.007
	$T_{\rm in}$	0.33 ± 0.04	$0.92^{+0.07}_{-0.06}$
	$R_{\rm in}\sqrt{\cos\theta}$ (km)	500^{+170}_{-100}	110^{+14}_{-12}
	Γ	1.8 ± 0.2	$2.9^{+0.3}_{-0.2}$
	$f_{\rm sc}$	$0.33^{+1.0}_{-0.07}$	$1.0^{\rm a}$
	χ^2/dof	172.9/189	367.4/314
MCD+NTHCOMP	$N_{\rm H}$ (10^{22} cm^{-2})	0.05 ± 0.02	$0.04^{+0.02}_{-0.01}$
	$T_{\rm in}$	0.33 ± 0.04	$0.4 \pm 0.1^{\rm b}$
	$R_{\rm in}\sqrt{\cos\theta}$ (km)	400^{+100}_{-70}	…
	$kT_e^{\rm d}$ (keV)	$100^{\rm a}$	$1.9^{+0.5}_{-0.3}$
	Γ	1.8 ± 0.2	1.9 ± 0.1
	χ^2/dof	173.2/189	310.7/313
OPTXAGNF ($a = 0$)	BH Mass ($M_\odot$)	22 ± 3	
	$\log L$ ($L_{\rm Edd}$)	0.02 ± 0.07	0.10 ± 0.08
	$R_{\rm cor}$ (r_g)	$100^{\rm a}$	$100^{\rm a}$
	τ	$100^{\rm a}$	15^{+7}_{-2}
	Γ	$1.60^{+0.04}_{-0.05}$	1.9 ± 0.3
	$kT_e^{\rm e}$ (keV)	0.5 ± 0.1	1.2 ± 0.2
	$f_{\rm pl}$	0.97 ± 0.01	0.4 ± 0.2
	χ^2/dof	500.6/502	
OPTXAGNF ($a = 0.998$)	BH Mass ($M_\odot$)	120 ± 20	
	$\log L$ ($L_{\rm Edd}$)	$-0.7^{+0.2}_{-0.1}$	$-0.6^{+0.2}_{-0.1}$
	$R_{\rm cor}$ (r_g)	15^{+3}_{-2}	15^{+12}_{-6}
	τ	24^{+76}_{-7} ^c	$100^{\rm a}$
	Γ	1.61 ± 0.06	2.0 ± 0.2
	$kT_e^{\rm e}$ (keV)	$1.0^{\rm a}$	$1.0^{\rm a}$
	$f_{\rm pl}$	$1.0^{\rm a}$	$0.71^{+0.01}_{-0.08}$
	χ^2/dof	510.6/503	

Notes.
[a] This parameter is frozen.
[b] This temperature is kT_{bb} in the NTHCOMP model because the MCD component is not included.
[c] The upper bound of τ is not well constrained.
[d] The electron temperature in the NTHCOMP model denotes the high-energy rollover. An exponential cutoff could be roughly estimated as $E_c = 2$–$3\ kT_e$.
[e] The electron temperature in the OPTXAGNF model denotes the soft excess caused by Comptonization. The electron temperature for the hard Comptonization component is fixed to 100 keV.

photon index of the hard Comptonization component (Γ), fraction ($f_{\rm pl}$) of the power below $R_{\rm cor}$ that is redistributed to the hard PL, and the redshift. We fit the X3 and X4 data sets simultaneously and tied the BH mass with each one, and assumed $N_{\rm H} = 7 \times 10^{20}$ cm^{-2} and $a = 0$. We found that the $R_{\rm cor}$ for these two data sets hit the hard limit. We therefore set $R_{\rm cor} = 100\ r_g$. A BH mass of $M_{\rm BH} = 22 \pm 3\ M_\odot$ can result in a good statistic (see Table 3). The luminosities are $1.1 \pm 0.2\ L_{\rm Edd}$ and $1.3 \pm 0.2\ L_{\rm Edd}$ for the X3 and X4 data sets, respectively. The Comptonized component has a high τ for both data sets, implying an optically thick corona. We also tried
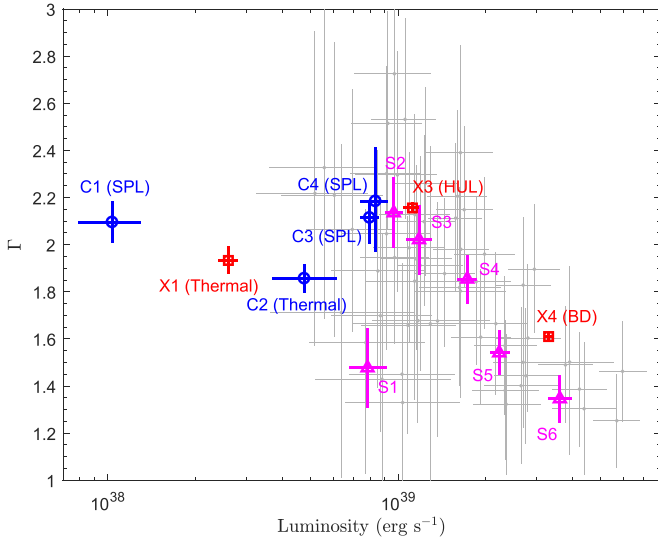
Figure 5. Photon indices obtained by all *Swift* individual observations (gray), *Chandra* (blue circle), *XMM-Newton* (red square), and stacked *Swift* observations (magenta triangle).

Figure 6. *Swift* stacked spectra and the best-fit MCD+PL model P9.

to set the BH spin to the maximum value of $a = 0.998$. In this fitting, R_{cor} is well constrained but τ is not. The fitting is insensitive to kT_e. Hence, we fixed it to 1 keV to account for the soft excess. We found that the BH mass is $120 \pm 20\,M_\odot$, six times larger than that of the $a = 0$ case. The corona has a radius of $\sim 15\,r_g$ for both the X3 and X4 spectra, roughly the same size as $\sim 100\,r_g$ of a $\sim 20\,M_\odot$ BH. Similar to the best-fit result for a non-spinning BH, a highly Comptonized, optically thick corona is required for both data sets.

3.3. Spectral Variability of Swift Observations

To obtain an overall hardness–intensity relationship, we fit the individual *Swift*, *Chandra*, and *XMM-Newton* data sets with a simple PL model and fixed N_H to $7 \times 10^{20}\,\mathrm{cm}^{-2}$ (see Figure 5). From the overall Γ–L relationship obtained from individual *Swift* observations, we found that Γ varied over a wide range when the luminosity is lower than $10^{39}\,\mathrm{erg\,s}^{-1}$, likely caused by the transition between the SPL and the high/soft states as seen in canonical BHXBs. In addition, Γ shows a break and a decreasing trend when the luminosity is higher than $10^{39}\,\mathrm{erg\,s}^{-1}$. We then stacked the *Swift* observations with similar luminosities and spectral behaviors to increase the signal-to-noise ratio (see Table 4 for definition and result). We fit the six data sets individually with N_H fixed to $7 \times 10^{20}\,\mathrm{cm}^{-2}$ using the Cash statistic. We also binned the spectra and fit them with the minimum χ^2 algorithm, and the results were fully consistent with those obtained from the Cash statistic. We fit the spectra with MCD+PL to get hints about the spectral behavior. We did not attempt to use more physical models to fit the *Swift* spectra due to a limited number of photons.

The S1 spectrum ($L < 10^{39}\,\mathrm{erg\,s}^{-1}$) is obviously disk-like. It can be well described by the MCD model with $kT_{in} = 1.3^{+0.3}_{-0.2}$ keV and $R_{in}\sqrt{\cos\theta} = 33^{+11}_{-9}$ km. We attempted to fit the S1 spectrum with the DiskPBB model and found $p = 0.7^{+0.2}_{-0.1}$, fully consistent with that of an MCD. The S2–S4 data sets are better described by a simple PL compared to the MCD. We obtained an anticorrelation between Γ and flux from these three data sets (see Figure 5). We tried to fit the spectra with the MCD+PL model, and the statistics were slightly improved.
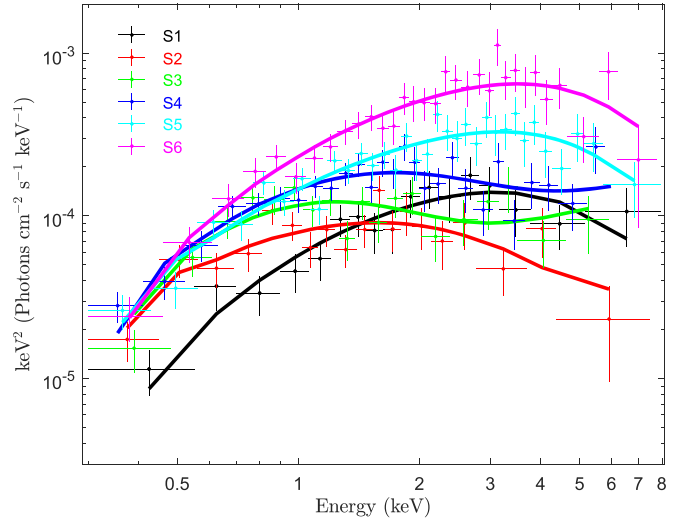
The best-fit MCD component suggested that the disk is cool with $kT_{in} \sim 0.5$ keV, and the inner radius is larger than the innermost stable circular orbit. We tried the DiskPBB model and yielded equally good statistics. The best-fit p-values are much smaller than those obtained from X4 and close to the hard limit of the DiskPBB model.

On the other hand, the S5 and S6 spectra are disk-like and can be well described with an MCD. Adding a PL component to S5 slightly improved the statistic but the change in the MCD component is limited and the PL component was not well constrained. The MCD fit of S5 has $kT_{in} = 1.4^{+0.4}_{-0.3}$ keV and $R_{in}\sqrt{\cos\theta} = 46^{+14}_{-13}$ km, similar to the MCD component in X4. This spectrum is equally well described with a p-free slim disk. The best-fit $p = 0.65^{+0.07}_{-0.07}$ is consistent with that obtained in the X4 data set but much closer to that of a standard MCD. For the S6 spectrum, adding a PL component or fitting p could not improve the fit statistic. The parameters of the PL components are not constrained, and the p-value is fully consistent with 0.75. We plot all of the stacked *Swift* spectra with the best-fit model in Figure 6 and rebin the spectral channels to have at least 5σ significance. It is clear that the spectral shape changes from PL-like to disk-like as flux increased when $L \gtrsim 10^{39}\,\mathrm{erg\,s}^{-1}$. S3 and S4 are similar to X3. They show a hint of a hard PL tail although the significance is low due to the limited energy range and low photon statistic. S5 and S6 are disk-like, but they do not have an obvious deviation from the S3 and S4 spectra below ~ 1 keV. This behavior is similar to that of X4, implying that the apparent disk-like spectrum could be misleading.

4. Discussion

4.1. Implications from the MCD+PL Model

4.1.1. Spectral Evolution of P9

During the canonical outburst, the X-ray spectrum of P9 switched between an MCD and a PL. The MCD spectra were observed in mid 2011 and mid 2012. The disk had an apparent inner radius of $R_{in}\sqrt{\cos\theta} \approx 50$ km and an inner-disk temperature $kT_{in} = 0.7$–0.9 keV. This radius corresponds to a true inner radius of 90 km after applying corrections for the color–temperature and inner boundary condition of an MCD

Table 4
Best-fit Spectral Parameters of Stacked *Swift* Spectra during the Ultraluminous Outburst

Bins	Luminosity Range (10^{39} erg s^{-1})	Model	$L_{0.3-10\ \mathrm{keV}}$[a] (10^{39} erg s^{-1})	L_{MCD} (10^{39} erg s^{-1})	$R_{\mathrm{in}}\sqrt{\cos\theta}$ (km)	kT_{in} (keV)	Γ or p	C^2/dof
S1	$L<1,\ \Gamma<1.8$	MCD	0.8 ± 0.1	0.8 ± 0.1	33^{+11}_{-9}	$1.3^{+0.3}_{-0.2}$	$\cdots$	143.9/167
S2	$L<1,\ \Gamma>1.8$	MCD+PL	0.86 ± 0.8	0.3 ± 0.1	150^{+120}_{-100}	$0.5^{+0.3}_{-0.1}$	1.9(5)	224.8/254
		DiskPBB		$\cdots$	<48	$1.1^{+0.4}_{-0.2}$	$0.53^{+0.04}_{-0.03}$[b]	223.2/255
S3	$L=1-1.3$	MCD+PL	1.2 ± 0.8	0.4 ± 0.2	300^{+180}_{-150}	$0.39^{+0.12}_{-0.08}$	$1.4^{+0.5}_{-0.9}$	149.1/184
		DiskPBB		$\cdots$	<25	$1.3^{+1.5}_{-0.4}$	$0.53^{+0.05}_{-0.04}$[b]	154.3/184
S4	$L=1.3-2$	MCD+PL	1.5 ± 0.2	$0.6^{+0.5}_{-0.3}$	150^{+90}_{-80}	$0.6^{+0.2}_{-0.1}$	$1.5^{+0.4}_{-0.9}$	258.3/267
		DiskPBB		$\cdots$	23^{+18}_{-21}	$1.4^{+0.8}_{-0.3}$	$0.56^{+0.04}_{-0.03}$[b]	264.8/267
S5	$L=2-3$	MCD+PL	2.2 ± 0.2	$1.7^{+0.3}_{-0.6}$	46^{+14}_{-13}	$1.4^{+0.2}_{-0.3}$	$2.3^{+6.2}_{-1.2}$	280.0/324
		DiskPBB		$\cdots$	34^{+20}_{-17}	$1.5^{+0.4}_{-0.2}$	$0.65^{+0.07}_{-0.05}$[b]	279.8/325
S6	$L>3$	MCD	$3.6^{+0.4}_{-0.3}$	$3.6^{+0.4}_{-0.3}$	56^{+11}_{-10}	$1.5^{+0.2}_{-0.1}$	$\cdots$	253.5/312

Notes.
[a] Derived from the best-fit model.
[b] This is the p-value of the p-free disk.

and assuming an inclination angle of 60° (Shimura & Takahara 1995; Kubota et al. 1998). Assuming a non-spinning BH, the mass can be estimated to be $\sim 10\,M_\odot$. For an extremely spinning BH, the apparent value corresponds to a BH mass of $\sim 60\,M_\odot$. In addition, the disk could be weakly Comptonized and result in a smaller R_{in} (Kubota & Makishima 2004). The above mass estimation represents the lower limit of the BH mass in P9. This indicates that P9 has a regular or massive stellar-mass BH. Its X-ray spectrum switched between the SPL and high/soft states of a canonical outburst before 2013 (Tetarenko et al. 2016).

When the luminosity exceeds 10^{39} erg s^{-1}, Γ shows a clear decreasing trend with the luminosity (see Figure 5), and the high-quality *XMM-Newton* spectra in this ultraluminous state cannot be well fit by single-component models. They are significantly different from those in the canonical outburst. When the luminosity is slightly higher than $L \approx 10^{39}$ erg s^{-1} (X3, S3, and S4), P9 has a cool disk and a hard PL tail. Moreover, the spectral curvature increases with flux when $L \gtrsim 2 \times 10^{39}$ erg s^{-1} (X4, S5, S6). These data sets can be described by disk-like spectral models.

As described in Section 1, the BD usually dominates the spectra of ULXs with $L \lesssim 3 \times 10^{39}$ erg s^{-1}, and those of ULXs with $L \gtrsim 3 \times 10^{39}$ erg s^{-1} showed two-component spectra like HUL and SUL (Gladstone et al. 2009; Sutton et al. 2013). However, some ULXs like NGC 1313 X-2 and Holmberg IX X-1 showed an inverse transition, i.e., an HUL spectrum in the low-luminosity state and a disk-like BD spectrum near their peak luminosities (Pintore & Zampieri 2012; Middleton et al. 2015; Luangtip et al. 2016). The BD feature of these sources is likely to be misclassified due to the strong spectral curvature caused by the highly optically thick Comptonized spectrum (Sutton et al. 2013). Similar to these two sources, P9 has an apparent inverse transition between these two states. However, the X4 light curve shows a significant variability dominated by the emission above 1 keV ($F_{\mathrm{var}} = 0.15(2)$ for 1–10 keV and $F_{\mathrm{var}} = 0.05(2)$ for 0.3–1 keV). It is difficult to interpret with a single slim disk model since the variability should be independent of the energy for a single emission component. Hence, we suggest that the apparent BD spectral shape observed in X4 consists of two components like NGC 1313 X-2 and Holmberg IX X-1.

4.1.2. Variability of the Disk Component

P9 evolved from the canonical BHXB regime to the ULX regime when its luminosity crossed the Eddington limit of a $\sim 10\,M_\odot$ BH. To obtain the disk evolution, we calculated the 0.3–10 keV luminosity of the disk to check its correlation with the inner-disk temperature. Assuming a fixed inner radius, the luminosity of a standard disk shows a positive correlation with the disk temperature:

$$L_{\mathrm{MCD}} = \frac{\pi\sigma G^2 M^2 T_{\mathrm{in}}^4}{6c_0^4 f_{\mathrm{col}}^4 c^4}, \qquad (2)$$

where σ is the Stefan–Boltzmann constant, M is the mass of the central compact object, $c_0 \approx 0.1067$, and f_{col}^4 is the color–temperature correction, which is usually larger than unity (Gierliński et al. 1999; Gierliński & Done 2004). Many ULXs (especially supersoft ones) show an anticorrelation between the disk luminosity and the temperature (see, e.g., Kajava & Poutanen 2009; Urquhart & Soria 2016). On the other hand, some ULXs show a positive correlation close to $L_{\mathrm{disk}} \propto T^4$ (Miller et al. 2003). Since P9 has both canonical and ultraluminous outbursts, it provides a unique chance to test the accretion disk model.

We collected the 0.3–10 keV luminosity of the MCD component and disk temperature from both the high/soft state (C2, X1, and S1), HUL state (X3, S3, S4, and possibly S2), and disk-like state in the ultraluminous outburst (X4, S5, and S6). We show the disk luminosity–temperature relation of P9 together with that of a BHXB, XTE J1550−564, in Figure 7. The disk configuration of P9 during the high/soft state in the canonical outburst (X1 and C2) was fully consistent with the thermal track of XTE J1550−564. We attempted to add an NTHCOMP component to these two data sets, but the Comptonized component contributed negligible emission. The apparent BD and MCD states during the ultraluminous outburst (X4, S1, S5, and S6) lie on the extension of the thermal track. This is likely a coincidence since they can also be well described by Comptonized models. The MCD component in the HUL-state clustering at the lower-left corner of this figure is similar to the ultraluminous branch of XTE J1550−564. However, P9 shows a much harder ($\Gamma \sim 1.6$–1.8)
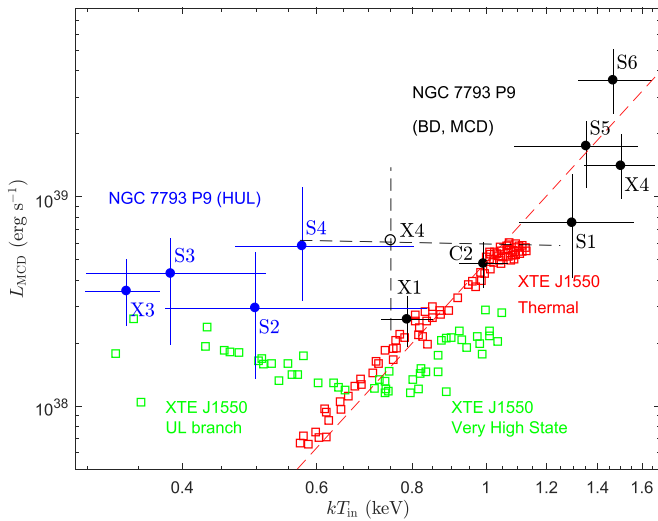
Figure 7. Comparison of the $kT_{\rm in}$–$L_{\rm MCD}$ relation between P9 and XTE J1550
−564 (Soria 2007). The red dashed line is the best-fit $L_{\rm MCD} \propto T_{\rm in}^4$ relation for
XTE J1550−564. The red squares are obtained from the high/soft state of XTE
J1550−564, and the green ones are from the SPL state and ultraluminous
branch. The black data points denote the thermal and BD states of P9, and the
blue ones denote the HUL spectral state. The black circle with the dashed line
is the best-fit thermal component of X4 spectra with a two-component model
containing an MCD and a PL with a high-energy cutoff.

PL tail compared to XTE J1550−564 ($\Gamma \sim 2.5$–2.8). The
presence of this state and the apparent disk-like state makes P9
a unique source among canonical BHXBs.

4.2. Implications of the Comptonized Disk

The simple MCD+PL model is helpful for classifying the
spectral states. The result suggests that the innermost region of
the accretion disk was covered by the Comptonized corona. We
further used physical models to deal with the coupling of both
the disk and the corona. We noticed that all of the spectra with
luminosities above $L \gtrsim 10^{39}\,{\rm erg\,s^{-1}}$, including X3, X4, and
S3–S6, show clear spectral difference above ∼1 keV (see
Figures 4 and 6). This implies that the mass accretion rate
during the ultraluminous outburst has no significant difference,
and the observed variability over $(1$–$5) \times 10^{39}$ erg s^{-1} is
dominated by the change of the Comptonized component. If we
use NTHCOMP to describe the Comptonized corona, then a
cool inner-disk temperature, a large re-estimated radius, a hard
PL with $\Gamma \sim 1.8$, and a large optical depth are necessary for
both X3 and X4 spectra. In contrast, X4 shows a higher
normalization and a clear cutoff at 4–6 keV. This implies that
the plasma temperature of the corona is hot at the beginning of
the ultraluminous outburst, and a huge amount of disk photons
are scattered to hard X-ray. As the corona temperature cools
down, fewer photons can be scattered to hard X-rays. The
spectrum shows a cutoff in the *XMM-Newton* energy range and
an apparently higher luminosity in 0.3–10 keV.

We also described the UL spectra with the OPTXAGNF
model. The BH mass can be estimated as ∼$20\,M_\odot$ for a non-
spinning BH or ∼$120\,M_\odot$ for an extremely fast spinning BH.
This result is a bit higher than that obtained from the simple
estimation based on the apparent inner-disk radius in the high/
soft state. In the case of $M_{\rm BH} \sim 20\,M_\odot$, most of the disk
emission below $R_{\rm cor}$ is scattered into the hard Comptonized
component ($f_{\rm pl} \sim 1$) and produces a hard PL with $\Gamma = 1.6$ in
X3 spectrum. When the X-ray luminosity increases to near the

peak of the ultraluminous outburst, significant power is emitted
in the low-temperature soft Comptonization component. This
result is consistent with the cooling of the corona, which is
implied from the NTHCOMP model. The luminosity is close to
or slightly higher than the Eddington luminosity, which
suggests that P9 belongs to the major ULX population: the
high-luminosity tail of BHXBs. Of course, we could not
exclude the explanation that X4 shows a slim disk since the
spectrum can be well fit by both the DiskPBB model and the
slim disk model. If this is true, the corona just fades away when
the luminosity is close to the peak. However, the short-term
variability is only observed above 1 keV in the X4 observation.
Therefore, the apparent BD spectrum likely contains two
components.

A BH with a mass of ∼120 $M_\odot$ can also produce the
observed spectra with a smaller coronal radius (in units of r_g).
The luminosity is roughly $0.2\,L_{\rm Edd}$, consistent with that of
canonical outbursts in BHXBs. If this is true, P9 is consistent
with a massive stellar-mass BH that was recently found via
gravitational wave observations (Abbott et al. 2016, 2017).
However, the hard PL tail observed in X3 is not expected in
canonical outbursts. Hence, this scenario is less favored.

4.3. Supercritical Accretion

The UL spectra can also be physically interpreted with the
supercritical accretion model. The inner disk is geometrically
thick, and an optically thick outflowing wind is blown. A
funnel-shaped cavity forms along the rotational axis of the BH
(King et al. 2001; Ohsuga & Mineshige 2007; Middleton
et al. 2015). In this case, the soft emission component is
contributed by the wind, and the hard emission component is
from the inner accretion disk or the accretion flow, although
detailed modeling is still under development (Poutanen
et al. 2007; Kajava et al. 2012). The beaming factor was
proportional to the mass accretion rate. Hence, the inclination
angle is expected to be low since the hard component
dominates the observed flux during the HUL state. The mass
accretion rate is maximum during the HUL state (X3), where
the beaming factor is large and we observed the innermost
accretion flow. When the mass accretion rate decreased, the
inner-disk temperature slightly cooled down and the beaming
factor decreased. The resulting spectrum is best described by a
BD if the emission from the wind becomes less dominant. As
the disk luminosity drops to sub-Eddington levels, we observe
a thin disk in the tail of the outburst. We attempted to fit the
hard component with DiskPBB in the X3 data set, but the disk
temperature is extremely high ($kT \sim 4$ keV) and the disk radius
is not well constrained. Therefore, this scenario is less favored
although not entirely excluded. Of course, a corona can
possibly form around the supercritical accretion disk and cause
a much more complex X-ray spectrum.

Finally, P9 shows the HUL spectrum when $L \approx 10^{39}$ erg s^{-1},
much lower than several genuine ULXs showing the same
spectral behavior (e.g., $(1$–$1.2) \times 10^{40}$ erg s^{-1} for Holmberg IX
X-1; Sutton et al. 2013). This could imply that those genuine
ULXs have much higher BH masses if the spectral state
classification only depends on the Eddington ratio. However,
the luminosity of a ULX can be strongly affected by the beaming
factor and viewing angle. An important counterexample is NGC
5907 ULX-1, which shows an HUL spectral behavior at
$L \gtrsim 10^{40}$ erg s^{-1}. Recently, it was found to be powered by a
neutron star (Israel et al. 2017a). Therefore, the spectral state and

the mass of the central compact object cannot be directly associated. The empirical luminosity range of the spectral states may stop being valid as the ULX sample grows. Comprehensively analyzing the timing and spectral behaviors of ULXs with next-generation X-ray telescopes and improving the supercritical accretion spectral model will be helpful for describing the accretion disk structure of ULXs.

5. Summary

We carried out a systematic analysis of the spectral variability of the newly discovered transient ULX NGC 7793 P9 with *Swift* XRT monitoring and dedicated *Chandra*, *XMM-Newton*, and *NuSTAR* observations. P9 is an LMXB and showed a canonical outburst behavior before 2013. The ultraluminous outburst after 2014 suggests that a BHXB can evolve to a ULX, supporting the scenario that some ULXs are powered by long-lasting super-Eddington outbursts. P9 is an important example bridging the BHXB and the ULX and shows the most fruitful spectral states among all ULXs. The spectral analysis implies that the compact object is a stellar-mass BH. The simple MCD+PL model suggests that P9 shows an ultraluminous branch, similar to XTE J1550−564. However, the spectrum is dominated by a much harder PL compared to XTE J1550−564. This is the feature of an HUL spectrum of a ULX. We suggest that the inner accretion disk is covered by a corona that scatters most of the inner-disk emission to a hard PL. In addition, P9 evolved to an apparent BD spectral state when $L \gtrsim 3 \times 10^{39}$ erg s^{-1} although it is likely misclassified due to the strong curvature of the Comptonized component. We suggested that the corona cools down but the disk component remains unchanged. The soft Comptonization dominated the observed spectrum. The spectral evolution can also be interpreted with the supercritical accretion model, although a detailed spectrum of this model is still under development. The theoretical models can be further tested by tracking the spectral evolution of more samples of transient ULXs.

Facilities: CXO (ACIS), XMM (MOS, PN), NuSTAR, Swift (XRT, UVOT).

ORCID iDs

Chin-Ping Hu (ID) https://orcid.org/0000-0001-8551-2002
Albert K. H. Kong (ID) https://orcid.org/0000-0002-5105-344X
C.-Y. Ng (ID) https://orcid.org/0000-0002-5847-2612

References

Abbott, B. P., Abbott, R., Abbott, T. D., et al. 2016, PhRvL, 116, 061102
Abbott, B. P., Abbott, R., Abbott, T. D., et al. 2017, PhRvL, 118, 221101
Anders, E., & Grevesse, N. 1989, GeCoA, 53, 197
Bachetti, M., Harrison, F. A., Walton, D. J., et al. 2014, Natur, 514, 202
Cash, W. 1979, ApJ, 228, 939
Crowther, P. A. 2013, MNRAS, 428, 1927
de Jager, O. C., Raubenheimer, B. C., & Swanepoel, J. W. H. 1989, A&A, 221, 180
Done, C., Davis, S. W., Jin, C., Blaes, O., & Ward, M. 2012, MNRAS, 420, 1848
Done, C., & Kubota, A. 2006, MNRAS, 371, 1216
Edelson, R., Turner, T. J., Pounds, K., et al. 2002, ApJ, 568, 610
Evans, P. A., Beardmore, A. P., Page, K. L., et al. 2007, A&A, 469, 379
Evans, P. A., Beardmore, A. P., Page, K. L., et al. 2009, MNRAS, 397, 1177
Feng, H., & Kaaret, P. 2006, ApJL, 650, L75
Feng, H., & Soria, R. 2011, NewAR, 55, 166
Frank, J., King, A., & Raine, D. (ed.) 2002, Accretion Power in Astrophysics (3rd ed.; Cambridge: Cambridge Univ. Press)
Fruscione, A., McDowell, J. C., Allen, G. E., et al. 2006, Proc. SPIE, 6270, 62701V
Gierliński, M., & Done, C. 2004, MNRAS, 347, 885
Gierliński, M., Zdziarski, A. A., Poutanen, J., et al. 1999, MNRAS, 309, 496
Gladstone, J. C., Roberts, T. P., & Done, C. 2009, MNRAS, 397, 1836
Hirano, A., Kitamoto, S., Yamada, T. T., Mineshige, S., & Fukue, J. 1995, ApJ, 446, 350
Hu, C.-P., Li, K. L., Kong, A. K. H., Ng, C.-Y., & Chun-Che Lin, L. 2017, ApJL, 835, L9
Israel, G. L., Belfiore, A., Stella, L., et al. 2017a, Sci, 355, 817
Israel, G. L., Papitto, A., Esposito, P., et al. 2017b, MNRAS, 466, L48
Kaaret, P., & Feng, H. 2009, ApJ, 702, 1679
Kaaret, P., & Feng, H. 2013, ApJ, 770, 20
Kaaret, P., Feng, H., & Roberts, T. P. 2017, ARA&A, 55, 303
Kajava, J. J. E., & Poutanen, J. 2009, MNRAS, 398, 1450
Kajava, J. J. E., Poutanen, J., Farrell, S. A., Grisé, F., & Kaaret, P. 2012, MNRAS, 422, 990
Kalberla, P. M. W., Burton, W. B., Hartmann, D., et al. 2005, A&A, 440, 775
Karachentsev, I. D., Grebel, E. K., Sharina, M. E., et al. 2003, A&A, 404, 93
Kawaguchi, T. 2003, ApJ, 593, 69
King, A. R. 2002, MNRAS, 335, L13
King, A. R., Davies, M. B., Ward, M. J., Fabbiano, G., & Elvis, M. 2001, ApJL, 552, L109
Kong, A. K. H., Hu, C.-P., Lin, L. C.-C., et al. 2016, MNRAS, 461, 4395
Kubota, A., & Done, C. 2004, MNRAS, 353, 980
Kubota, A., & Makishima, K. 2004, ApJ, 601, 428
Kubota, A., Tanaka, Y., Makishima, K., et al. 1998, PASJ, 50, 667
Lau, R. M., Kasliwal, M. M., Bond, H. E., et al. 2016, ApJ, 830, 142
Luangtip, W., Roberts, T. P., & Done, C. 2016, MNRAS, 460, 4417
Middleton, M. J., Heil, L., Pintore, F., Walton, D. J., & Roberts, T. P. 2015, MNRAS, 447, 3243
Middleton, M. J., Sutton, A. D., Roberts, T. P., Jackson, F. E., & Done, C. 2012, MNRAS, 420, 2969
Miller, J. M., Fabbiano, G., Miller, M. C., & Fabian, A. C. 2003, ApJL, 585, L37
Mineshige, S., Hirano, A., Kitamoto, S., Yamada, T. T., & Fukue, J. 1994, ApJ, 426, 308
Mitsuda, K., Inoue, H., Koyama, K., et al. 1984, PASJ, 36, 741
Motch, C., Pakull, M. W., Soria, R., Grisé, F., & Pietrzyński, G. 2014, Natur, 514, 198
Ohsuga, K., & Mineshige, S. 2007, ApJ, 670, 1283
Pannuti, T. G., Schlegel, E. M., Filipović, M. D., et al. 2011, AJ, 142, 20
Pavlovskii, K., Ivanova, N., Belczynski, K., & Van, K. X. 2017, MNRAS, 465, 2092
Pintore, F., & Zampieri, L. 2012, MNRAS, 420, 1107
Poutanen, J., Lipunova, G., Fabrika, S., Butkevich, A. G., & Abolmasov, P. 2007, MNRAS, 377, 1187
Radburn-Smith, D. J., de Jong, R. S., Seth, A. C., et al. 2011, ApJS, 195, 18
Rappaport, S. A., Podsiadlowski, P., & Pfahl, E. 2005, MNRAS, 356, 401

Read, A. M., & Pietsch, W. 1999, A&A, 341, 8
Shimura, T., & Takahara, F. 1995, ApJ, 445, 780
Soria, R. 2007, Ap&SS, 311, 213
Steiner, J. F., Narayan, R., McClintock, J. E., & Ebisawa, K. 2009, PASP, 121, 1279
Sutton, A. D., Roberts, T. P., & Middleton, M. J. 2013, MNRAS, 435, 1758
Tetarenko, B. E., Sivakoff, G. R., Heinke, C. O., & Gladstone, J. C. 2016, ApJS, 222, 15

Tully, R. B., Courtois, H. M., & Sorce, J. G. 2016, AJ, 152, 50
Urquhart, R., & Soria, R. 2016, MNRAS, 456, 1859
Vierdayanti, K., Mineshige, S., & Ueda, Y. 2010, PASJ, 62, 239
Walton, D. J., Fürst, F., Bachetti, M., et al. 2016, ApJL, 827, L13
Wilms, J., Allen, A., & McCray, R. 2000, ApJ, 542, 914
Zdziarski, A. A., Johnson, W. N., & Magdziarz, P. 1996, MNRAS, 283, 193
Życki, P. T., Done, C., & Smith, D. A. 1999, MNRAS, 309, 561